Electronic Properties of Nanodiamond Decorated Graphene
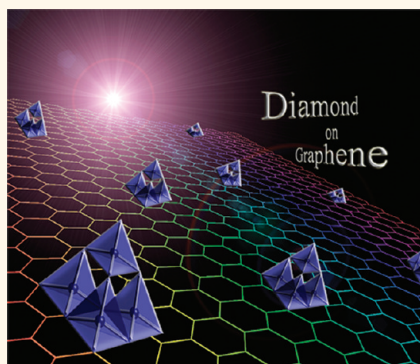
Yu Wang,[†,‡,¶] Manu Jaiswal,[†,‡,§,¶,#] Ming Lin,[⊥] Surajit Saha,[‡,§,∥] Barbaros Özyilmaz,[‡,§,∥] and Kian Ping Loh[†,‡,*]

[†]Department of Chemistry, National University of Singapore, 3 Science Drive 3, 117543, Singapore, [‡]Graphene Research Centre, National University of Singapore, 2 Science Drive 3, 117542, Singapore, [§]Department of Physics, National University of Singapore, 2 Science Drive 3, 117542, Singapore, [⊥]Institute of Materials Research and Engineering, 3 Research Link, 117602, Singapore, and [∥]NanoCore, National University of Singapore, Singapore 117576, Singapore. [¶]These authors contributed equally to this work. [#]Present address: Department of Physics, Indian Institute of Technology Madras, Chennai 600036, India.

Since its exfoliation in 2004,[1] graphene's unique electronic properties have attracted widespread attention.[2,3] The carriers in graphene behave as massless chiral Dirac fermions that propagate without backscattering.[3,4] These electronic properties can be significantly transformed and diversified by functionalization and chemical modification of the graphene lattice.[5−8] Such modifications allow a band gap to be realized in the energy spectrum of graphene when the sublattice symmetry is broken.[7] The attachment of defect sites is also known to locally modify the curvature of graphene lattice, leading to interesting physical phenomenon such as local strain, spin−orbit coupling, and magnetic correlations, which are relevant to spintronic and magnetoelectronic applications.[6,9−13] However, the nanoscale control of the adsorption of adatoms or molecules to the graphene lattice is non-trivial. In the case of plasma-induced hydrogenation or fluorination of intact graphene, a thermodynamic clustering of the defects often occurs.[5,6,14−17] However, the adsorbed hydrogen or fluorine atoms are unstable after prolonged period. Another strategy is to create an ensemble of chemically modified domains by the chemical fusion of nanoparticles to graphene, which can induce local defects or strained domains. Compared to adsorbed atoms or molecules, the interfacial bonding can be robust and the density of these nanoparticles can be controlled to create pockets of hybridized area, where the local bonding can be changed from sp^2 to sp^3. Furthermore, attachment of atoms or nanoparticles introduces diverse functionalities particularly with reference to magnetic correlations with the carriers in graphene, which are strongly dependent on the nature of adsorbed adatom, its distribution density, and position of electronic energy levels.[18,19]

Certain adatoms also cause significant charge transfer doping,[6] leading to coexistence of conducting high-energy channels from the sp^3-rich area together with the intact sp^2 graphene-rich areas, and this doping effect is detrimental to imparting insulating properties to the film. In this work, we investigate the chemical fusion of nanodiamond (ND) particles to graphene by growing graphene on ND-coated copper substrate during chemical vapor deposition (CVD). Low-temperature magnetotransport experiments performed on graphene/ND films transferred to SiO$_2$ substrates reveal

ABSTRACT

The electronic properties of graphene sheets decorated with nanodiamond (ND) particles have been investigated. The chemical fusion of ND to the graphene lattice creates pockets of local defects with robust interfacial bonding. At the ND-bonded regions, the atoms of graphene lattice follow sp^3-like bonding, and such regions play the role of conduction bottlenecks for the percolating sp^2 graphene network. The low-temperature charge transport reveals an insulating behavior for the disordered system associated with Anderson localization for the charge carriers in graphene. A large negative magnetoresistance is observed in this insulating regime, and its origin is discussed in the context of magnetic correlations of the localized charge carriers with local magnetic domains and extrinsic metal impurities associated with the ND.
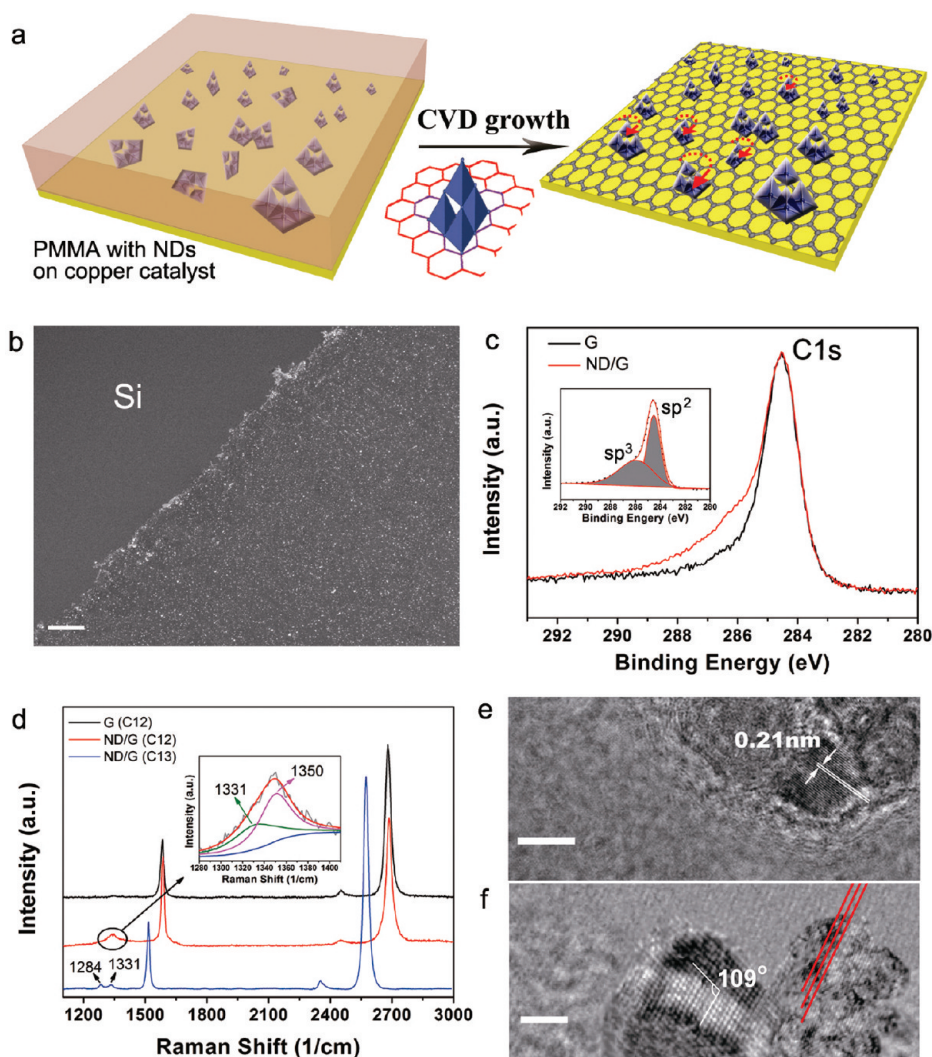
Figure 1. Synthesis method, microscopy observations, and spectroscopic analysis of the ND/G hybridized structure. (a) Schematic diagram for the growth of the hybrid nanostructure of ND and graphene. (b) SEM image of ND/G film on Si substrate. Scale bar is 1 μm. (c) XPS measurements verify the presence of ND and graphene. The inset shows sp^2 and sp^3 peaks of the C1s core—shell in the ND/G structure by fitting peaks. Schematic model of the interface, side view. (d) Raman spectra (514 nm excitation) analysis of ND/G system. The D peak of graphene can be separated from the diamond characteristic peak by using C^{13} isotope labeling. (e) Typical TEM image of the ND particles. The spacing of the lattice fringe in the diamond crystallites is about 0.21 nm. Scale bar is 5 nm. (f) HRTEM images of the hybrid nanostructure at the interface. The interfaces between ND and graphene are ($1\bar{1}1$) and ($\bar{1}11$), intersecting at an angle of 109° and/or in parallel each other. Scale bar is 2 nm.

that the NDs create conduction bottlenecks for the percolating sp^2 graphene network, leading to insulating behavior. The charge carriers are localized by disorder, and the conduction at low carrier densities can be described by a two-dimensional (2D) variable-range hopping (VRH) mechanism. Besides introducing localization, the detonation-synthesized purified NDs are also a source of magnetism in the form of trace magnetic impurities. Besides, the possibility of carbon magnetism from diamond—graphene attachment is quite interesting since defects within individual nanodiamond grains are already debated to induce ferromagnetic order.[20] In the insulating regime, strong modulations of the resistance are observed in the presence of magnetic fields, which can be

attributed to interactions of the localized charge carriers with magnetic impurities or with atomic magnetic moments.

Growth and Characterization. The graphene film was grown on copper foil coated with fluorinated ND particles. During CVD growth, the graphene film grows at the interface between the copper and ND. A schematic of the growth of the ND/G hybridized structure is shown in Figure 1a. The coupling of carbon nanotubes and ND particles to form a hybrid nanocarbon system has been demonstrated in previous experiments, where the growth of NDs required the presence of defects on the nanotube.[21,22] In our experiment, the copper foil substrate presents the platform needed for growth of graphene, while the ND particles allow for
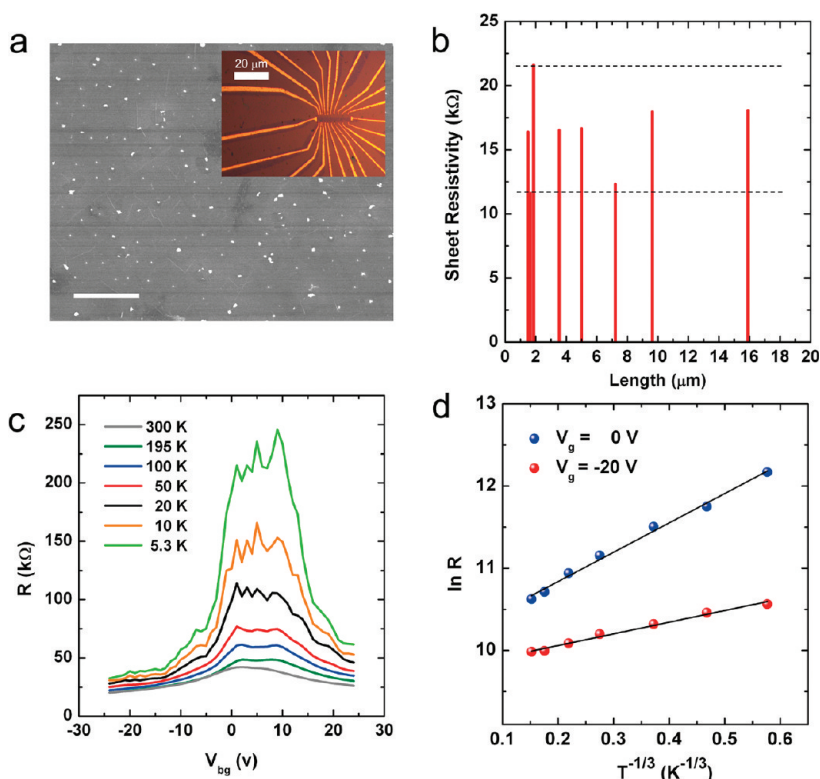
Figure 2. Charge transport measurements on micrometer-size graphene/ND devices. (a) SEM image of graphene/ND film showing the distribution of ND clusters. Scale bar is 1 μm [inset: optical image of graphene/ND device]. (b) Sheet resistivity *vs* length for 3 μm wide adjacent devices. (c) Resistance *vs* V_{bg} at different temperatures from T = 2.5 to 300 K. (d) Plot of ln R *vs* $T^{-1/3}$ for V_g = 0 V (blue), −20 V (red).

the formation of sp^3 carbon inclusions following the fusion of ND with graphene. Fluorinated NDs are used for the following reasons: (i) it can be dispersed readily in solution, thus allowing the homogeneous seeding of graphene with discrete NDs, as shown by the scanning electron micrograph (SEM) in Figure 1b; (ii) fluorinated NDs have increased reactivity toward C−C bond formation with diamond at high temperature. The density of NDs on the Cu surface is readily controlled by varying the speed of spin-coating, and this allows us to adjust the electrical channel of graphene devices by changing the average distance between NDs (Supporting Information Figure S2).

X-ray photoelectron spectroscopy (XPS) was performed to reveal the nature of the chemical bonding among atoms in the nanostructure. Figure 1c shows that the C1s spectrum can be deconvoluted into two peaks at 284.5 and 285.8 eV. These two components correspond to the sp^2-bonding carbon (graphene) and sp^3-bonding carbon (diamond), respectively. The coexistence of ND and graphene is also evidenced by the Raman spectrum (514 nm) in Figure 1d, which shows an overlapped peak with contribution from the characteristic diamond peak at 1331 cm^{-1} and graphene D peak induced by defects at 1350 cm^{-1}, prominent graphene G ($\sim$1587 cm^{-1}) and 2D ($\sim$2688 cm^{-1}) band.[23,24] Micro-Raman analysis of the region shows that the 2D band exhibits a blue shift

of 8 cm^{-1} compared to pure graphene without ND, due perhaps to the bond-angle disorder and compressive stress at the sp^2:sp^3 composite interface.[25] To distinguish the overlapped Raman peaks, ^{13}C isotopically labeled graphene was grown on the ND-coated copper foil using ^{13}CH$_4$ as carbon source. Before the growth, the sample was annealed at 500 °C under H$_2$ for 30 min in order to exclude the effect of PMMA as ^{12}C carbon source. The result shows that the D peak of graphene (^{13}C) is red-shifted upon isotope enrichment, while the diamond peak is still at 1331 cm^{-1} in Figure 1d. High-resolution transmission electron microscopy (HRTEM) measurements and electron energy loss spectroscopy (EELS) were employed to study the interface between NDs and graphene (see Supporting Information). A typical TEM image of the ND particles in Figure 1e reveals that the spacing of the lattice fringe is about 0.21 nm, which agrees well with diamond {111} planes.[26] Diamond crystallites with a diameter of around 3−6 nm are either surrounded by amorphous carbon (the particles located at noninterface region) or embedded directly on the graphene matrix. In Figure 1f, a set of diamond {111} planes in the ND crystal can be seen to orient parallel to the graphene (0001) planes, although at this point, microscopic information about the detailed interface cannot be obtained.

Charge Transport. Charge transport measurements were performed on lithographically patterned four-terminal

devices after transferring the graphene/ND films onto SiO_2/Si wafers. Figure 2a shows an SEM image of NDs on the graphene surface, and ND clusters are distributed with separations of a few hundred nanometers. The room temperature sheet resistivity of several 3 μm wide graphene/ND regions is plotted as a function of length L, varying from $L = 1$ to 16 μm in Figure 2b. On micrometer scale devices, the effect of NDs is averaged-out, and the variations in the resistivity are within a factor of 2, which can be attributed to carrier density inhomogeneity on graphene as well as some variations in the ND defect density. All devices were found to be slightly hole-doped with the charge neutrality point (CNP) typically shifted by 0–15 V, suggesting the lack of significant charge transfer doping. In contrast, dilute hydrogenated graphene shows significant hole doping.[27] In comparison to pristine graphene, the presence of ND clusters increases the sheet resistivity at any given carrier density by a small factor (2–4). The temperature-dependent transport of a 2 μm square channel is plotted in Figure 2c, and it reveals an insulating behavior for the system, particularly at the CNP where the resistance increases by an order in magnitude. The temperature dependence of resistance, both near CNP and away from CNP, is well described by the two-dimensional (2D) variable range hopping (VRH) form, $R \propto \exp(T_0/T)^{1/3}$, with $T_0 = 13.8/k_B N(E_F)\xi^2$, as shown in the semilogarithmic plot in Figure 2d.[6,28−30] Here T_0 is the characteristic temperature, $N(E_F)$ is the density of states at Fermi level, and ξ is the localization length. While estimating $N(E_F)$, the disorder-induced voltage width of the conductivity minimum is also taken into consideration: $n(\Delta V_g) = C_{bg}(\Delta V_g^2 + V_{dis}^2)^{1/2}/e$, where C_{bg} is the back-gate capacitance, ΔV_g is the gate-bias measured from CNP, and V_{dis} is the disorder-induced width of the CNP plateau. From the slope of temperature-dependent resistance, the value of localization length is found to be $\xi \sim 160$ nm near CNP, and it increases for carrier densities away from CNP. This value of ξ correlates remarkably with the typical separations between ND clusters, suggesting that the distribution of sp^3-type carbon inclusions arising from fusion of NDs can control the transport length scale at low carrier densities.[28]

Next, we note that for graphene samples with a random distribution of atomic-scale defects, $\rho > h/e^2$ near CNP is always associated with strong localization at low temperature ($T < 100$ K): an increase in resistance by several orders in magnitude, with T_0 values ranging from 200 to 400.[6,28,29] The graphene/ND films also show significant insulating behavior, but the obtained T_0 value at CNP is lower (45−100) than what would normally be expected from the large resistivity. To further illustrate this difference, we obtained a second estimate of the localization length based on the elastic scattering length, L_e.[28] The value obtained, $\xi(L_e) = [\sigma_D h/(2e^2(\pi n)^{1/2})]\exp(\sigma_D h/e^2) \sim 21$ nm, using the high

temperature ($T = 300$ K) CNP Drude conductivity value, σ_D. While this second estimate is certainly crude, the large difference between ξ and $\xi(L_e)$ deserves a discussion as to which represents the true value of localization length. We first note that the localization length obtained from VRH fits depends on the slope of the temperature dependence of resistance and is not sensitive to the actual value of *resistivity* of the sample.[30] On the other hand, the absolute magnitude of resistivity directly appears in the *exponential* term of the localization length function that is based on elastic scattering length, making it highly sensitive to the exact value of resistivity. One plausible explanation of the difference in the two estimates for localization length is related to the rather inhomogenous distribution of ND defect pockets in our system on length scales that are comparable to transport length scales. This defect distribution in our system is notably different from that of atomically adsorbed adatoms, except when the latter shows tendency for strong clustering. In this scenario, the resistivity originating from the percolating sp^2 graphene network could dominate the temperature response, while the sp^3-dominated domains will not have an appreciable contribution to the temperature dependence, although their presence will enhance the effective geometrical resistivity when they are considered as components of two-dimensional two-resistor networks.[31] The crude estimate of localization based on the magnitude sheet resistivity can only be applied if the distribution of defects is homogeneous.

Magnetotransport. The low-temperature magnetotransport in the graphene/ND system is plotted in Figure 3, and it reveals significant negative magnetoresistance (MR) that reaches −70% at $B = 8$ T, without saturation as shown for sample 1 [see the inset in Figure 3b]. The negative MR is maximized in the vicinity of the CNP, where localization effects dominate. Upon increasing the temperature, the magnetoresistance effects progressively diminish. Such magnetoresistance behavior in the strong localization regime has been associated with quantum interference phenomenon,[32−34] similar to the weak localization interference phenomenon seen in graphene with low density of defects.[27−29,35−38] For strong localization, the MR originating from various quantum interference effects is expected to reach a value close to saturation at magnetic fields defined by $B_{sat} \sim h/(e\xi^2 T_0/T) \sim 0.15$ T at $T = 10$ K, where ξ is the localization length related to the presence of sp^3-type carbon inclusions discussed in the above section.[29] In our experiment, however, saturation does not happen even for magnetic fields up to 8 T, and furthermore, the magnitude of MR is also very large. This points to a different origin for the MR. The large magnetic fields (several Tesla range) involved for saturation raises the possibility that the MR originates from the interaction of localized carriers with spin-polarized impurity states.[18,19] It remains to be
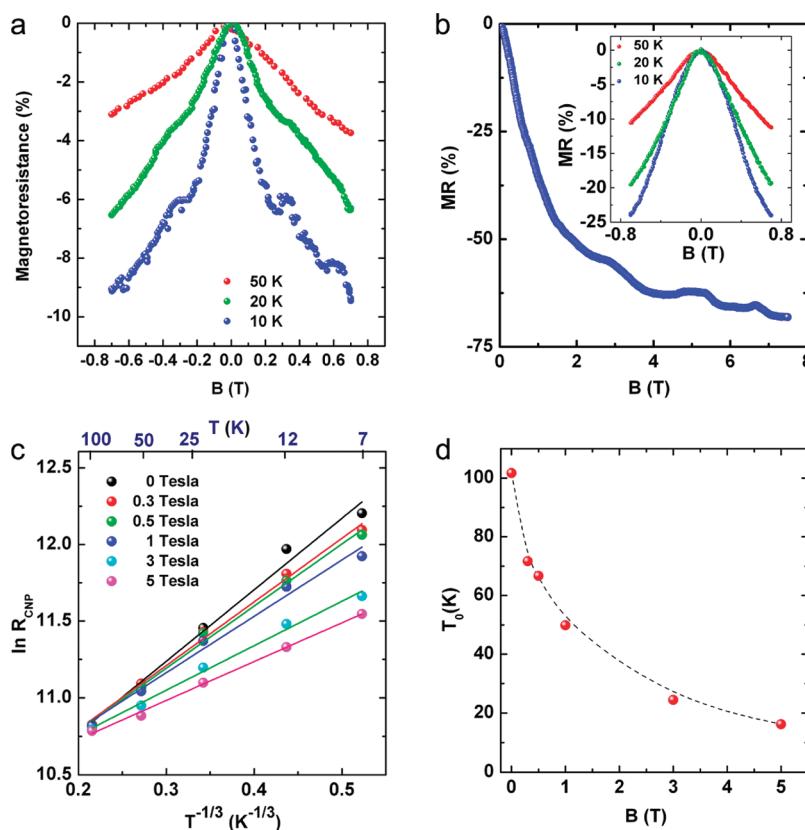
Figure 3. Magnetotransport measurements on micrometer-size graphene/ND devices. (a) Low-field magnetotransport: MR *vs* B at $V_g = -20$ V (away from CNP) for different temperatures: $T = 10$ K (blue), 20 K (green), and 50 K (red) for sample 1. (b) High-field magnetotransport: MR *vs* B at $V_g = 0$ V (near CNP), $T = 10$ K [inset: MR *vs* B at $V_g = 0$ V (near CNP) at low field for different temperatures] for sample 1. (c) VRH plot for sample 2: ln R *vs* $T^{-1/3}$ at CNP for different magnetic fields ($B = 0$, 0.3, 0.5, 1, 3, 5 T). (d) Characteristic temperature T_0 *vs* magnetic field for sample 2 (the dotted line is a guide for the eye).

evaluated from first-principle calculations whether the attachment of nanodiamond to graphene lattice can indeed produce local magnetic moments with magnetic ordering. Such possibilities have been suggested for a variety of adatom moments including hydrogen adatoms,[13,39−41] although direct transport measurements are lacking with the possible exception of dilute fluorinated graphene.[29] The attachment of NDs on graphene is particularly interesting since the defect-related intrinsic magnetism has been debated within the individual ND grain itself.[20,42] However, the experimental verification of this possibility in the graphene/ND system is limited by the fact that NDs synthesized by detonation process invariably contain a small fraction of extrinsic magnetic impurities. As a result, magnetism is an extrinsic phenomenon associated with NDs, with saturation magnetization of M_s of the order 0.01 emu/g.[42] The estimated fraction of Fe impurity in the ND powder is 0.1%, and their presence is also verified in graphene/ND films from proton-induced X-ray emission (PIXE) scans (see Supporting Information). Therefore, magnetic impurities appear to be the more likely candidate to explain the strong MR in our system. Small concentrations of metallic magnetic impurities are already known to significantly influence the high-field magnetotransport in organic systems, and they are known to induce Kondo-like behavior in

carbon nanotube systems.[43] Typically, large magnetic fields ($B > 6$ T) are needed for reaching saturation magnetization, both for ferromagnetic and for superparamagnetic responses from impurities present in NDs, as demonstrated in previous magnetization studies on ND powder.[42] The temperature dependence of CNP resistance is plotted at different magnetic fields ($B = 0$ to 5 T) for sample 2 in Figure 3c. The temperature dependence of the resistance can be described by the expression for generalized 2D-VRH that includes the influence of magnetic field:[19]

$$\rho = \rho_0 \exp(T_0(H)/T)^{1/3}$$

where $T_0(H) \propto \xi_{eff}^2$ is the magnetic-field-dependent characteristic temperature. The magnetic field dependence of $T_0(H)$ is plotted in Figure 3d. When the spins associated with magnetic impurities are fully polarized under external field, the exchange interaction with the localized carriers decreases their binding energy.[19] This allows delocalization of the charge carriers, which persists beyond magnetic fields of 8 T.

FUTURE OUTLOOK AND CONCLUSION

One approach to clarify the exact role of individual ND grains in the transport properties of these hybrid films is to pattern graphene nanostructures that
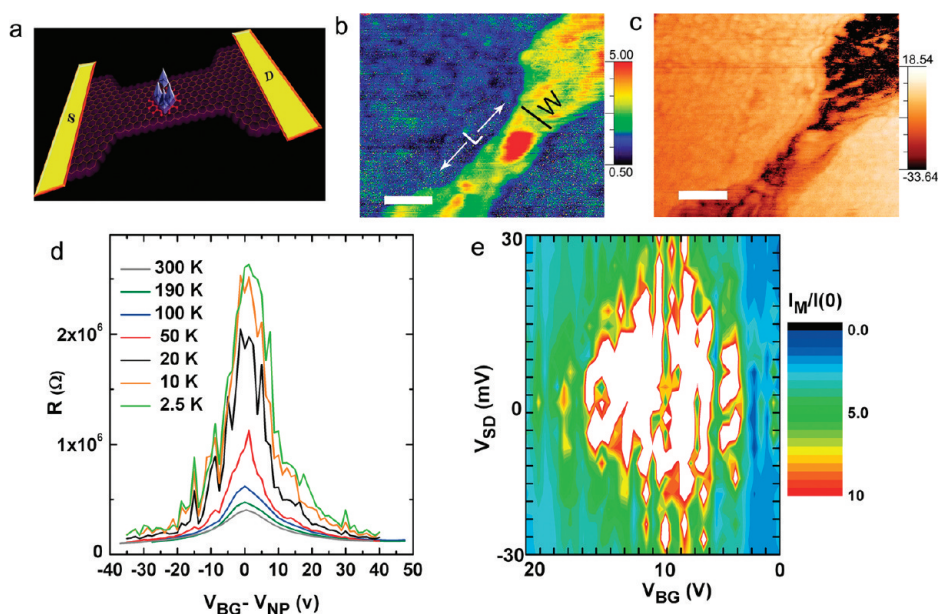
Figure 4. Magnetotransport measurements on graphene/ND nanostructures. (a) Schematic of the concept of intersecting GNRs with ND defect hotspots. (b) Tapping mode AFM topography image of graphene constriction intersecting a cluster of nanodiamonds (in red, lateral size ~70 nm). Scale bar is 100 nm. (c) Tapping mode AFM phase image of the same GNR/ND device. (d) Resistance *vs* $V_{bg} - V_{NP}$ at different temperatures from T = 2.5 to 300 K. (e) Two-dimensional plot of current through the device under 8 T magnetic field, normalized to zero-field value. Region shaded in white corresponds to a current enhancement $I_M/I(0) > 10$.

intersect them (see schematic in Figure 4a). The transport in such devices is expected to be dominated by the interface of graphene and ND. Our preliminary data from such nanostructures indicate that significant negative MR can exist in the energy window of strong localization (see Figure 4d,e). A 2D plot of the current ratio $I(8\ T)/I(0\ T)$ measured in sample GNC-1 from two different sweeps at T = 2.5 K is shown as a function of source-drain bias and back-gate voltage in Figure 4e. The region shaded in white in Figure 4e corresponds to a current enhancement by more than a factor of 10 (*i.e.*, negative MR more than −90%), and it defines the energy-space window of strong localization ($\Delta V_{bg} \sim 15$ V and a source-drain bias window of $\Delta V_{sd} \sim 60$ mV). These values appear to be significant when compared to the localization effect of edges alone in pristine graphene nanoconstrictions of comparable width.[44−48] More experiments are needed to clarify if extrinsic magnetic impurities can be associated with individual grains/clusters of NDs and whether the ND−graphene coupling itself comprises magnetized atomic scale moments (see Supporting Information Figures S8 and S9 for additional data).

To summarize, we demonstrate that the chemical fusion of nanodiamonds (NDs) to graphene lattice introduces localized pockets of sp^3 regions. The presence of NDs influences the transport by causing conduction bottlenecks and increases the sheet resistance. The temperature and magnetic-field-dependent transport reveal the presence of strong localization, particularly at low carrier densities. Charge transport in this system involves a subtle interplay involving both the sp^2- and sp^3-rich regions. The graphene/ND film shows significant negative magnetoresistance at low temperature, and the likely origin of this lies in magnetic correlations of the localized carriers with trace amounts of extrinsic magnetic impurities that are characteristic of detonation-synthesized NDs. Further experiments are needed to clarify the exact origin of the magnetic centers in graphene/ND films since the possibility of atomic magnetic moments at the sites bonded to ND cannot be overlooked.[19] This may require different approaches to bind diamond and graphene lattices. Finally, we note that even nonmagnetic transition metal atoms adsorbed in the vicinity of graphene lattice have been predicted to show significant gate-tunable magnetism upon hybridizing with the graphene lattice.[18] For experiments involving disordered graphene systems with non-magnetic metal adatoms,[18,49] our results provide useful comparison.

METHODS

Materials Preparation. In a typical experiment, 5 mg of fluorinated ND (4−5 nm) (International Technology Center) was first added to 50 mL of poly(methyl methacrylate) PMMA (MicroChem Corp. 950 PMMA A5, 5% in anisole) and then dispersed by ultrasonication for 1 h. The PMMA-coated ND dispersion was centrifuged at 13 000 rpm for 120 min. The upper 80% of the supernatant was carefully decanted to collect the ND.

A ~2 cm × 2 cm Cu foil (25 μm thick, 99.999% purity, Alfa Aesar) was used as the substrate for CVD growth. The Cu foil was first annealed at 1030 °C with flowing 2 sccm H_2 for 1 h. After cooling to room temperature under H_2 atmosphere, 20 mL of PMMA-coated F-ND solution was deposited on the Cu foil by spin-coating. The density of the PMMA-coated ND on the Cu foil can be controlled by changing the speed of spin-coating on copper foil from 500 to 3000 rpm, as seen in Figure S2 (see Supporting Information). The as-prepared PMMA-coated F-NDs/Cu was baked at 150 °C for 5 min and then transferred to a tubular furnace for the growth of nanodiamond/graphene (ND/G) hybridized structure.

Chemical Vapor Deposition. In the CVD growth of ND/G hybridized structure, PMMA plays two roles: (1) fixing the F-NDs on copper foil and (2) solid carbon source for the growth of graphene.[50] Before the growth of ND/G, the CVD furnace was heated to 950 °C in vacuum. After the temperature became stable, PMMA/F-NDs/Cu foil was introduced into the furnace and a gas mixture of CH_4 (8 sccm), Ar (100 sccm), and H_2 (30 sccm) at ~8.5 Torr was introduced. After 20 min of growth, the system was cooled to room temperature under H_2. Although PMMA can be used as carbon source for the growth of graphene, CH_4 was also introduced as carbon source in order to ensure the continuity of ND/G film.

Characterization of ND/G Film. The as-produced ND/G films were characterized using high-resolution transmission electron microscopy (HR-TEM, FEI Titan, 80 kV). After TEM images were obtained, selected area electron diffraction and high-resolution electron energy loss spectroscopy (EELS) were also performed. The Raman spectra were measured with a WITEC CRM200 Raman system at room temperature. The excitation source is 514 nm with a laser power below 0.1 mW to avoid laser-induced heating of the sample. The spot size of 514 nm laser light is estimated to be 500 nm.

Fabrication and Measurement of Devices. Graphene/nanodiamond hybrid system grown by chemical vapor deposition (CVD) was transferred onto Si/SiO$_2$ (300 nm) substrate after etching the copper foil with 25 mM ammonium persulfate solution for ~6 h. Then, 100 μL of 4% poly(methyl methacrylate) (MicroChem, MW = 950 K) anisole solution was spin-coated on substrates at 4000 rpm and baked at 180 °C for 2 min. Devices were patterned by electron-beam lithography (FEI/Nova Nano SEM), and this was followed by development of PMMA with methyl isobutyl ketone (MIBK) and isopropyl alcohol (1:1) solution. Thermal evaporation of 5 nm Cr/30 nm Au was followed by lift-off in acetone and rinsing in IPA. In a subsequent e-beam lithography step, an etch mask was patterned and the graphene was exposed to 20 W, 20 sccm oxygen plasma (RIE NTI-2312) for 20 s after resist development. The devices were annealed in 10% Ar/H_2 at 200 °C for 3 h to reduce the amount of organic residue.

Electrical measurements on wire-bonded graphene/ND devices were performed using four-terminal geometry. For graphene/ND nanoconstriction devices, the measurements were performed in two-terminal geometry. For typical resistance measurements, a small low-frequency (~13.3 Hz) AC current (10 nA) was applied through the samples and the voltage drop was measured using a Stanford SRS-830 lock-in amplifier. The highly doped silicon wafer serves as the gate electrode with a 300 nm silicon oxide as the dielectric layer. The charge carrier density in graphene was tuned by applying a gate voltage through Keithley 6430 subfemtoamp source meter. The maximum gate leakage was restricted to 1−1.5 nA current. Low-temperature magnetoresistance in the range T = 2.5 to 300 K was measured in a Cryogenics variable temperature system equipped with a 9 T superconducting magnet. The magnetic field was applied perpendicular to the plane of the sample. Differential conductance measurements were performed using the standard combination of Keithley 6221 AC−DC current−source synchronized with Keithley 2182A nanovoltmeter.

REFERENCES AND NOTES

1. Novoselov, K. S.; Geim, A. K.; Morozov, S. V.; Jiang, D.; Zhang, Y.; Dubonos, S. V.; Grigorieva, I. V.; Firsov, A. A. Electric Field Effect in Atomically Thin Carbon Films. *Science* **2004**, *306*, 666–669.
2. Zhang, Y.; Tan, Y.-W.; Stormer, H. L.; Kim, P. Experimental Observation of the Quantum Hall Effect and Berry's Phase in Graphene. *Nature* **2005**, *438*, 201–204.
3. Neto, A. H. C.; Guinea, F.; Peres, N. M. R. The Electronic Properties of Graphene. *Rev. Mod. Phys.* **2009**, *81*, 109–162.
4. Sarma, S. D.; Adam, S.; Hwang, E. H.; Rossi, E. Electronic Transport in Two Dimensional Graphene. *Rev. Mod. Phys.* **2011**, *83*, 407.
5. Sofo, J. O.; Chaudhari, A. S.; Barber, G. D.; Graphane, A Two-Dimensional Hydrocarbon. *Phys. Rev. B* **2007**, *75*, 153401.
6. Elias, D. C.; Nair, R. R.; Mohiuddin, T. M. G.; Morozov, S. V.; Blake, P.; Halsall, M. P.; Ferrari, A. C.; Boukhvalov, D. W.; Katsnelson, M. I.; Geim, A. K.; *et al.* Control of Graphene's Properties by Reversible Hydrogenation: Evidence for Graphane. *Science* **2009**, *323*, 610–613.
7. Schwierz, F. Graphene Transistors. *Nat. Nanotechnol.* **2010**, *5*, 487–496.
8. Ci, L.; Song, L.; Jin, C.; Jariwala, D.; Wu, D.; Li, Y.; Srivastava, A.; Wang, Z. F.; Storr, K.; Balicas, L.; *et al.* Atomic Layers of Hybridized Boron Nitride and Graphene Domains. *Nat. Mater.* **2010**, *9*, 430–435.
9. Levy, N.; Burke, S. A.; Meaker, K. L.; Panlasigui, M.; Zettl, A.; Guinea, F.; Neto, A. H. C.; Crommie, M. F. Strain-Induced Pseudo-Magnetic Fields Greater Than 300 T in Graphene Nanobubbles. *Science* **2010**, *329*, 544–547.
10. Yeh, N.-C.; Teague, M. L.; Wu, R. T.; Yeom, S.; Standley, B.; Boyd, J.; Bockrath, M. W. Strain-Induced Pseudo-Magnetic Fields and Charging Effects on CVD-Grown Graphene. *Surf. Sci.* **2011**, *605*, 1649–1656.
11. Neto, A. H. C.; Guinea, F. Impurity-Induced Spin−Orbit Coupling in Graphene. *Phys. Rev. Lett.* **2009**, *103*, 026804.
12. Soriano, D.; Munoz-Rojas, F.; Fernandez-Rossier, J.; Palacios, J. J. Hydrogenated Graphene Nanoribbons for Spintronics. *Phys. Rev. B* **2010**, *81*, 165409.
13. Zhou, J.; Wang, Q.; Chen, X. S.; Kawazoe, Y.; Jena, P. Ferromagnetism in Semihydrogenated Graphene Sheet. *Nano Lett.* **2009**, *9*, 3867–3870.
14. Shytov, A. V.; Abanin, D. A.; Levitov, L. S. Long-Range Interaction between Adatoms in Graphene. *Phys. Rev. Lett.* **2009**, *103*, 016806.
15. Nair, R. R.; Ren, W.; Jalil, R.; Riaz, I.; Kravets, V. G.; Britnell, L.; Blake, P.; Schedin, F.; Mayorov, A. S.; Yuan, S.; *et al.* Fluorographene: A Two-Dimensional Counterpart of Teflon. *Small* **2010**, *6*, 2877–2844.
16. Wang, Y.; Xu, X. F.; Lu, J.; Lin, M.; Bao, Q. L.; Özyilmaz, B.; Loh, K. P. Toward High Throughput Interconvertible Graphane-to-Graphene Growth and Patterning. *ACS Nano* **2010**, *4*, 6146–6152.
17. Ryu, S.; Han, M. Y.; Maultzsch, J.; Heinz, T. F.; Kim, P.; Steigerwald, M. L.; Brus, L. E. Reversible Basal Plane Hydrogenation of Graphene. *Nano Lett.* **2008**, *8*, 4597–4602.
18. Uchoa, B.; Kotov, V. N.; Peres, N. M. R.; Neto, A. H. C. Localized Magnetic States in Graphene. *Phys. Rev. Lett.* **2008**, *101*, 026805.
19. Rappoport, T. G.; Uchoa, B.; Neto, A. H. C. Magnetism and Magnetotransport in Disordered Graphene. *Phys. Rev. B* **2009**, 80.
20. Talapatra, S.; Ganesan, P. G.; Kim, T.; Vajtai, R.; Huang, M.; Shima, M.; Ramanath, G.; Srivastava, D.; Deevi, S. C.; Ajayan,

P. M. Irradiation-Induced Magnetism in Carbon Nano-structures. *Phys. Rev. Lett.* **2005**, *95*, 097201.

21. Barnard, A. S.; Terranova, M. L.; Rossi, M. Density Functional Study of H-Induced Defects as Nucleation Sites in Hybrid Carbon Nanomaterials. *Chem. Mater.* **2005**, *17*, 527–535.

22. Terranova, M. L.; Orlanducci, S.; Fiori, A.; Tamburri, E.; Sessa, V.; Rossi, M.; Barnard, A. S. Controlled Evolution of Carbon Nanotubes Coated by Nanodiamond: The Realization of a New Class of Hybrid Nanomaterials. *Chem. Mater.* **2005**, *17*, 3214–3220.

23. Malard, L. M.; Pimentaa, M. A.; Dresselhaus, G.; Dresselhaus, M. S. Raman Spectroscopy in Graphene. *Phys. Rep.* **2009**, *473*, 51–87.

24. Ferrari, A. C.; Robertson, J. Interpretation of Raman Spectra of Disordered and Amorphous Carbon. *Phys. Rev. B* **2000**, *61*, 14095–14107.

25. Egerton, R. F. *Electron Energy Loss Spectroscopy in the Electron Microscope*, 2nd ed.; Plenum: New York, 1996.

26. Lee, S. T.; Peng, H. Y.; Zhou, X. T.; Wang, N.; Lee, C. S.; Bello, I.; Lifshitz, Y. A Nucleation Site and Mechanism Leading to Epitaxial Growth of Diamond Films. *Science* **2000**, *287*, 104–106.

27. Jaiswal, M.; Lim, C. H. Y. X.; Bao, Q.; Toh, C. T.; Loh, K. P.; Ozyilmaz, B. Controlled Hydrogenation of Graphene Sheets and Nanoribbons. *ACS Nano* **2011**, *5*, 888–896.

28. Moser, J.; Tao, H.; Roche, S.; Alsina, F.; Torres, C. M. S.; Bachtold, A. Magnetotransport in Disordered Graphene Exposed to Ozone: From Weak to Strong Localization. *Phys. Rev. B* **2010**, *81*, 205445.

29. Hong, X.; Cheng, S.-H.; Herding, C.; Zhu, J. Colossal Negative Magnetoresistance in Dilute Fluorinated Graphene. *Phys. Rev. B* **2011**, *83*, 085410.

30. Zabrodskii, A. G. The Coulomb Gap: The View of the Experimenter. *Philos. Mag. B* **2001**, *81*, 1131.

31. Bianco, B.; Giordano, S. Electrical Characterization of Linear and Non-linear Random Networks and Mixtures. *Int. J. Circuit Theory Appl.s* **2003**, *31*, 199–218.

32. Nguyen, V. L.; Spivak, B. Z.; Shklovskii, B. I. Tunnel Hops in Disordered Systems. *Sov. Phys. - JETP* **1985**, *62*, 1021.

33. Jaiswal, M.; Wang, W.; Fernando, K. A. S.; Sun, Y.-P.; Menon, R. Charge Transport in Transparent Single-Wall Carbon Nanotube Network and Devices. *J. Phys.: Condens. Matter* **2007**, *19*, 446006.

34. Entin-Wohlman, O.; Imry, Y.; Sivan, U. Orbital Magneto-conductance in the Variable-Range-Hopping Regime. *Phys. Rev. B* **1989**, *40*, 8342.

35. Horsell, D. W.; Tikhonenko, F. V.; Gorbachev, R. V.; Savchenko, A. K. Weak Localization in Monolayer and Bilayer Graphene. *Philos. Trans. R. Soc. A* **2008**, *366*, 245–250.

36. Chen, J.-H.; Cullen, W. G.; Jang, C.; Fuhrer, M. S.; Williams, E. D. Defect Scattering in Graphene. *Phys. Rev. Lett.* **2009**, *102*, 236805.

37. McCann, E.; Kechedzhi, K.; Fal'ko, V. I.; Suzuura, H.; Ando, T.; Altshuler, B. L. Weak-Localization Magnetoresistance and Valley Symmetry in Graphene. *Phys. Rev. Lett.* **2006**, *97*, 146805.

38. Yu, Q.; Jauregui, L. A.; Wu, W.; Colby, R.; Tian, J.; Su, Z.; Cao, H.; Liu, Z.; Pandey, D.; Wei, D.; *et al.* Control and Character-ization of Individual Grains and Grain Boundaries in Graphene Grown by Chemical Vapour Deposition. *Nat. Mater.* **2010**, *10*, 443–449.

39. Xie, L.; Wang, X.; Lu, J.; Ni, Z.; Luo, Z.; Mao, H.; Wang, R.; Wang, Y.; Huang, H.; Qi, D.; *et al.* Room Temperature Ferromagnetism in Partially Hydrogenated Epitaxial Graph-ene. *Appl. Phys. Lett.* **2011**, *98*, 193113.

40. Soriano, D.; Leconte, N.; Ordejon, P.; Charlier, J.-C.; Palacios, J.-J.; Roche, S. Magnetoresistance and Magnetic Ordering Fingerprints in Hydrogenated Graphene. *Phys. Rev. Lett.* **2011**, *107*, 016602.

41. Leconte, N.; Soriano, D.; Roche, S.; Ordejon, P.; Charlier, J.-C.; Palacios, J. J. Magnetism-Dependent Transport Phe-nomenon in Hydrogenated Graphene: From Spin-Splitting to Localization Effects. *ACS Nano* **2011**, *5*, 3987–3992.

42. Levin, E. M.; Fang, X. W.; Bud'ko, S. L.; Straszheim, W. E.; McCallum, R. W.; Schmidt-Rohr, K. Magnetization and 13C NMR Spin-Lattice Relaxation of Nanodiamond Powder. *Phys. Rev. B* **2008**, *77*, 054418.

43. Kim, G. T.; Choi, E. S.; Kim, D. C.; Suh, D. S.; Park, Y. W.; Liu, K.; Duesberg, G.; Roth, S. Magnetoresistance of an Entangled Single-Wall Carbon-Nanotube Network. *Phys. Rev. B* **1998**, *58*, 16064.

44. Terres, B.; Dauber, J.; Volk, C.; Trellenkamp, S.; Wichmann, U.; Stampfer, C. Disorder Induced Coulomb Gaps in Graph-ene Constrictions with Different Aspect Ratios; arXiv: 1011.2091v2, **2011**.

45. Molitor, F.; Stampfer, C.; Guttinger, J.; Jacobsen, A.; Ihn, T.; Ensslin, K. Energy and Transport Gaps in Etched Graphene Nanoribbons. *Semicond. Sci. Technol.* **2010**, *25*, 034002.

46. Bai, J.; Cheng, R.; Xiu, F.; Liao, L.; Wang, M.; Shailos, A.; Wang, K. L.; Huang, Y.; Duan, X. Very Large Magnetoresistance in Graphene Nanoribbons. *Nat. Nanotechnol.* **2010**, *5*, 655–659.

47. Han, M. Y.; Ozyilmaz, B.; Zhang, Y.; Kim, P. Energy Band-Gap Engineering of Graphene Nanoribbons. *Phys. Rev. Lett.* **2007**, *98*, 206805.

48. Oostinga, J. B.; Sacepe, B.; Craicun, M. F.; Morpurgo, A. F. Magneto-Transport through Graphene Nanoribbons; arXiv:1003:2994v1, **2010**.

49. Fert, A.; Levy, P. M. Spin Hall Effect Induced by Resonant Scattering on Impurities in Metals. *Phys. Rev. Lett.* **2011**, *106*, 157208.

50. Sun, Z.; Yan, Z.; Yao, J.; Beitler, E.; Zhu, Y.; Tour, J. Growth of Graphene from Solid Carbon Source. *Nature* **2010**, *468*, 549–552.